An Efficient Noninvasive Neuromodulation Modality for Overactive Bladder Using Time Interfering Current Method

Jiho Lee, Eunkyoung Park, Wonok Kang, Yuri Kim, Kyu-Sung Lee, and Sung-Min Park*

***Abstract*— *Objective:* The present study aimed to evaluate a new tibial nerve stimulation (TNS) modality, which uses interferential currents, in terms of the stimulation electric field penetration efficiency into the body and physiological effectiveness. *Methods: In silico* experiments were performed to analyze the penetration efficiency of proposed interferential current therapy (ICT). Based on this, we performed *in vivo* experiments to measure excitation threshold of ICT for the tibial nerve, which is related to stimulation field near the nerve. Regarding analysis of the physiological effectiveness, *in vivo* ICT–TNS was performed, and changes in bladder contraction frequency and voiding volume were measured. The penetration efficiency and physiological effectiveness of ICT were evaluated by comparison with those of conventional TNS using transcutaneous electrical nerve stimulation (TENS). *Results:* Simulation results showed that ICT has high penetration efficiency, thereby generating stronger field than TENS. These results are consistent with the *in vivo* results that nerve excitation threshold of ICT is lower than that of TENS. Moreover, ICT–TNS decreased contraction frequency and increased voiding volume, and its performance was profound compared with that of TENS–TNS. *Conclusion:* The proposed ICT is more efficient in inducing the stimulation field near the tibial nerve placed deep inside the body compared with conventional TENS and shows a good clinical effectiveness for TNS. *Significance:* The high efficiency of ICT increases the safety of noninvasive neurostimulation; therefore, it has clinical potential to become a promising modality for TNS to treat OAB and other peripheral neurostimulations.**

***Index Terms*— Interferential current therapy, Tibial nerve stimulation, Transcutaneous electrical nerve stimulation, Noninvasive neurostimulation, Overactive bladder syndrome**

I. Introduction

OVERACTIVE bladder syndrome (OAB) is a symptom of neurogenic bladder considered as a complex urinary urgency [1, 2]. OAB is a highly prevalent disease (the *Current Bladder Dysfunction Reports* estimated that approximately 16% of the population of the USA experience it [3]) that burdens patients with decreasing quality of life [4, 5]. This abnormal voiding reflex can be caused by either damage of the inhibitory central nervous system or sensitization of the peripheral system [6]. Antimuscarinic drugs, such as oxybutynin, are well known to effectively correct neurogenic abnormalities and are thus the dominant treatment for OAB. However, such drugs have side effects, such as low effectiveness or inhibition of other organs such as the mouth [7-9]. For patients who do not benefit from drug therapy, neurostimulation has been suggested, with proven clinical effects. Although sacral nerve stimulation (SNS) is the most common and main neurostimulation technique for OAB, some limitations have been reported, such as stimulator implantation issues [10].

Electrical tibial nerve stimulation (TNS) has been demonstrated as an effective, simple, low-risk alternative to SNS [11, 12]. The selected TNS site, located near the posterior ankle, is easily accessible compared with the surgery required for the neurostimulation method of SNS [13-15]. Two TNS stimulating strategies are known: invasive and noninvasive methods. Noninvasive TNS using skin-attached electrodes is safer and more convenient than the invasive method requiring needle insertion [16]. The widely used method for noninvasive TNS is transcutaneous electrical nerve stimulation (TENS).

However, conventional TENS method exhibits poor penetration efficiency of the stimulation electric field because TENS generates extremely low inner-body field intensity compared with its strong near-skin field. The low penetration efficiency of TENS may result in common stimulation side effects, such as skin redness, burn, or an undesired sensation such as pain [17]. This is because the low penetration efficiency of TENS hampers the stimulation current flowing inside the body, resulting in most of the stimulation energy being attenuated proximal to the skin. To mitigate this safety burden,

This work was supported by the MSIT (Ministry of Science and ICT), Korea, under the ICT Consilience Creative program (IITP-2019-2011-1-00783) supervised by the IITP (Institute for Information & Communications Technology Promotion), the Basic Science Research Program through the National Research Foundation of Korea (NRF) funded by the Ministry of Science and ICT (NRF-2017R1A5A1015596), and the Technology Innovation Program (or Industrial Strategic Technology Development Program) (20001841, Development of System for Intelligent Context-Aware Wearable Service based on Machine Learning) funded by the Ministry of Trade, Industry & Energy (Korea). Jiho Lee and Eunkyoung Park contributed equally to this work *(Corresponding author: Sung-Min Park.)*

J. Lee, Y. Kim and *S. Park are with Department of Creative IT Engineering, Pohang University of Science and Technology, 37673, Republic of Korea. (e-mail: ezo15@postech.ac.kr)

W. Kang is with School of Interdisciplinary Bioscience and Bioengineering, Pohang University of Science and Technology, 37673, Republic of Korea.

E. Park and K. Lee are with Department of Urology and Smart Healthcare Research Institute, Samsung Medical Center, Sungkyunkwan University School of Medicine, 06351, Seoul, Republic of Korea, Seoul, 06351, Republic of Korea.

the stimulation intensity can be lowered; however, such lowering may compromise the clinical effectiveness.

To overcome the aforementioned limitations and achieve a high penetration efficiency, in the present study, we propose a new strategy for noninvasive TNS based on interferential current therapy (ICT), thereby providing high-field penetration efficiency and minimizing attenuation in the subcutaneous area [18, 19]. ICT has been considered only as a focusing modality for electrical stimulations; however, it has a better potential for improving the field penetration efficiency using high frequency carrier signals. Grossman *et al.* [20] reported on this potential of ICT by applying it to the brains of mice. However, we believe that ICT can maximize its benefits for peripheral nerve stimulation applications, such as TNS, rather than brain stimulation, where regions that are too deep are targeted. To quantitatively analyze our pioneering approach toward ICT, we performed extensive computational analysis of the field penetration efficiency of ICT. The corresponding animal experiments measured the nerve excitation ability of ICT, which is strongly related to the field generated near the nerve. With regard to the physiological performance of ICT, we practically demonstrated the physiological effectiveness of ICT by performing *in vivo* experiments measuring change in bladder activity after ICT–TNS. Furthermore, we evaluated the field penetration efficiency and physiological effectiveness of ICT by comparing them with those of TENS.

II. Methods

A. Concept of ICT for Noninvasive Neuromodulation

The electrical impedances in body tissue decrease as the frequency of applied external current increases; consequently, the penetration depth of applied current becomes deeper and the induced field inside the body increases. The conventional TENS methods utilize low-frequency current, ultimately resulting in the inherent low-penetration issue. Moreover, currents induced by the TENS spread on the body from the source, exhibiting poor localization for the stimulation. The ICT method overcomes this issue using the amplitude-modulation of high-frequency signals. Applying high-frequency signals that differ only by a slight frequency level (e.g., $f_1 = 2$ kHz, $f_2 = 2.01$ kHz), a low-frequency beat envelope ($\Delta f = f_1 - f_2 = 10$ Hz) is created by current interference. If the beat frequency is sufficiently low for neurons to respond, interfering currents can then evoke the nervous system as pure low-frequency stimulation [21, 22]. The high-frequency ICT carrier facilitates penetration, and its low-frequency envelope facilitates substantial nerve stimulation. In other words, the high-frequency modulated by the ICT has the simultaneous advantages of avoiding the body impedance effect and evoking the nervous system.

B. Waveform Design for ICT and TENS

Waveform parameters for TENS and ICT are as follows: (1) TENS (200-μs pulse width/10-Hz frequency/square waveform), (2) ICT (2 kHz + 2.01 kHz double sources). These parameters of TENS were reportedly effective in bladder inhibition and useful in treating OAB [12, 23, 24]. The 2-kHz carrier frequency for ICT stimulation was selected by benchmarking a research demonstrating the effectiveness of ICT from a neuron cell to the brain tissue level [20]. The 10-Hz beat frequency of ICT was chosen to match the stimulation frequency of TENS. Therefore, using these parameters, we justified a fair comparison between the proposed ICT–TNS method and the clinically applied TENS–TNS method in the real world.

Fig. 1 shows the conceptual waveform difference between ICT and TENS. Phase synchronization of ICT at 50 and 150 ms showed positive interference, and desynchronization at 0, 100, and 200 ms showed negative interference. The 100-ms period (= 10 Hz) envelope signal by the interferences of ICT can stimulate the nervous system and elicit a neural response. In contrast, although TENS typically comprises zero intensity signal, short pulses appear at 100 and 200 ms. The stimulation period of TENS and ICT is 100 ms; however, the ICT waveform uses the full time of 100 ms for stimulation, whereas the TENS waveform uses only 200 μs of 100 ms for the same stimulation.

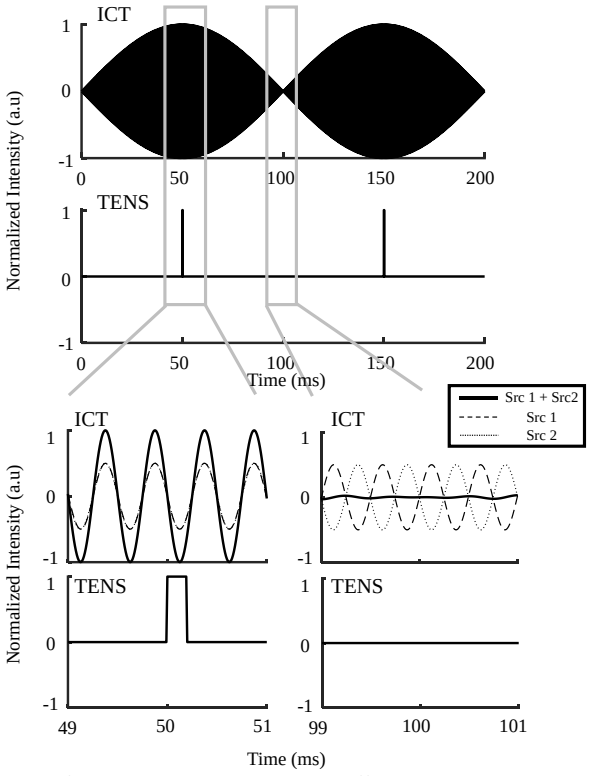

Fig. 1. Waveform and stimulation modality differences between TENS and ICT. TENS has a 200-μs pulse width and 10-Hz frequency. ICT has a −2-kHz carrier frequency and 10-Hz interfering (envelope) frequency (Src 1: 2 kHz, Src 2: 2.01 kHz). Unlike TENS, ICT utilizes the 100-ms envelope gnerated by the interference beat.

C. Simulation Platform Validation (Phantom Experiment)

A biomedical electromagnetic simulator (Sim4Life, Zürich MedTech AG) was used to predict the EM field distribution on an *in vivo* tissue. Prior to its use, the simulator was extensively validated via *in vitro* measurements.

1) Electromagnetic Simulation Theory

From the electroquasistatic assumption,

$$E = -\nabla\phi. \quad (1)$$

We can solve Laplace's equation under the Dirichlet constant voltage boundary condition without the source current:

$$\nabla \cdot [(\sigma + j\omega\varepsilon)\nabla\phi] = 0, (\because J_{\text{source}} = 0), \quad (2)$$

where ε is the permittivity, σ is the effective (equivalent) electrical conductivity, and ω is the angular frequency [25, 26]. The potential for each voxelized element with the finite element method was obtained by solving Eq. (2) and the corresponding electric field was calculated by Eq. (1).

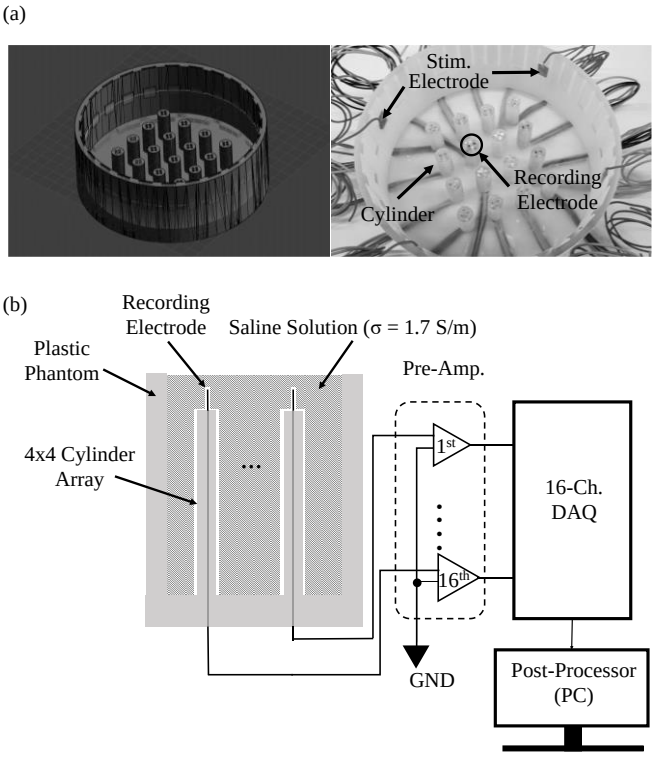

Fig. 2. (a) 3D modeled (left) and fabricated phantom (right). (b) Schematic overview for the measurement system of *in vitro* phantom experiment.

2) Phantom Fabrication

Fig. 2(a) shows a 78-mm radius plastic container (M2R-CL, VisiJet®) with a 4 × 4 cylinder array, fabricated as a phantom design using a 3D CAD tool (SolidWorks, Dassault Systèmes SOLIDWORKS Corp.). Overall, 16 cylinders with 1-cm diameter were placed at every 2 cm. Four point-voltage recording electrodes were placed at the four cardinal directions (left, right, top, and bottom) of each cylinder. Two square-shaped stimulating stainless-steel electrodes (1 × 1 cm) were positioned on the circumference of the container at a 45° angle to be fully soaked. The container was filled with a 0.9% NaCl physiological saline solution [27]. The conductivity of the filing solution was σ = 1.7 S/m, as measured using a conductivity meter (YK-43CD, Lutron).

3) In Vitro and In Silico Phantom Experiments

For phantom experiments, a constant voltage of 3.04 V at 1 kHz was applied using a waveform generator (33220A, Agilent) between the stimulating electrodes. The effective load voltage was directly measured through an oscilloscope (DPO 3032, Tektronix) to compensate for the impedance matching errors. Fig. 2(b) presents the experiment's schematic measurement system. For each cylinder, four voltage values were measured from each recording electrode using a differential voltage DAQ system (NI 9220, National Instruments). The four measured values were averaged after acquisition and total 16 voltage values per cylinder were obtained.

For simulation, the 3D CAD file of the phantom was imported into the simulator. Virtual stimulating electrodes were placed at the same location as in the *in vitro* experiments. The container body's conductivity was set as the ideal perfect dielectric of 0 S/m. The filling solution was assigned a conductivity of 1.7 S/m and a relative permittivity of $\varepsilon_r = 76.5$, which corresponds to measured saline conductivity and water permittivity. The constant voltages of 3.04 V and GND were applied to the stimulating electrodes. To estimate the open space, zero paddings and 0 V were applied on the outside boundary.

TABLE I
MATERIAL PROPERTIES FOR SIMULATION AT 10 AND 2 KHZ

Material	10 Hz	
	Conductivity σ (S/m)	Relative Permittivity ε_r [a]
Air[b]	0	1
Skin	2×10^{-4}	1136
Fat	1.2207×10^{-2}	7.9735×10^{6}
Muscle	0.20197	2.57×10^{7}
Blood	0.7	5260
Gel	0.6	76.5

Material	2 KHz	
	Conductivity σ (S/m)	Relative Permittivity ε_r [a]
Air	0	1
Skin	2.0023×10^{-4}	1135.3
Fat	2.3048×10^{-2}	10308
Muscle	0.32953	168020
Blood	0.7	5257
Gel	0.6	76.5

[a]The relative permittivity $\varepsilon_r = \varepsilon/\varepsilon_0$.
[b]Background

D. In Silico TENS and ICT Experiments

3D human and rat anatomical models were imported into the simulator with the parameters shown in Table I [28, 29]. The ICT and TENS stimulators were compared in terms of electric field distribution. The 26-year-old Korean female model *Yoon-sun cV3.1*, constructed with magnetic resonance imaging and computed tomography images, was used as the human model [30, 31]. A *big male rat* (Sprague–Dawley, 567 g) was used as the rat model [32]. Fig. 3 shows the virtual electrodes positioned for each TENS and ICT in the rat and human models (see Fig. 13). For the rat model, the size of the electrodes was 2.5 mm wide × 2.5 mm long × 1 mm high. The conductive gel had the same width and length of the electrodes but the

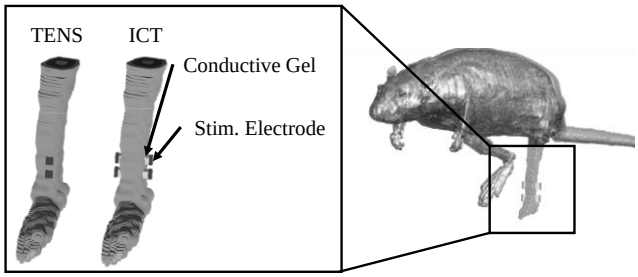

Fig. 3. 3D rat model used for *in silico* rat experiments. Stimulating electrodes for TENS and ICT were placed near the posterior ankle. The electrodes were placed to target the same stimulating position.

thickness of gel ranged from 0.5 to 2 mm due to uneven surface of the skin. For the human model, the electrode size was 1 cm wide × 1 cm long × 1 mm high and the gel thickness ranged from 0.5 to 1 cm.

For TENS modeling, a single source consisting of two stimulating electrodes was vertically placed on the posterior part of the right ankle. A conductive gel was placed between each electrode and the skin. Tissue conductivity, which depends on the operating frequency, was set at 10 Hz, which is known to inhibit the micturition reflex (MR) [23, 33, 34]. The load voltage between electrodes was 10 V. The outside boundary was set to 0 V/m with the Neumann condition. The simulated electric field was extracted as a result. Specifically, the electric field along the z-axis (Ez), which is parallel to the tibial nerve spreading, was selected because nerves are more sensitive to parallel field than to orthogonal field [35].

For ICT modeling, four different electrodes were positioned near the ankle, allocating two electrodes per source. Tissue parameters were set at a 2 kHz frequency (because 2 kHz and 2.01 kHz are nearly similar). After simulating each source, the effective interfering envelope intensity of 10 Hz frequency was calculated, and its intensity (Ez_{env}) was approximated as follows:

$$\begin{aligned} Ez_{env} &= 2\min(|Ez_1|, |Ez_2|) \\ &= \big||Ez_1 + Ez_2| - |Ez_1 - Ez_2|\big|, \end{aligned} \tag{3}$$

where Ez_1 and Ez_2 are the z-axis electric field components of each source.

E. Stimulation Thresholds of TENS and ICT

1) Concept of Stimulation Threshold

To quantitatively assess the nerve excitation ability of a noninvasive stimulation modality, we introduce the concept of *stimulation threshold*, which is defined as the minimum stimulus intensity for the occurrence of nerve excitation. Therefore, a higher stimulation threshold indicates that it is more difficult for the noninvasive stimulation to induce nerve excitation.

2) Stimulation Threshold for the Tibial Nerve

The anatomical connection between the tibial nerve and hallux muscle induces motor actions, such as toe tremor, when the tibial nerve is effectively evoked due to stimulation. This acute motor response of hallux during TNS is a good clinical indicator of excitation of the tibial nerve due to noninvasive stimulation [23].

3) In Vivo Measurement of Stimulation Threshold

In vivo experiments were performed on rats sampled from the population described above (6 male Sprague–Dawley rats) to compare the stimulation threshold between TENS and ICT. Under isoflurane anesthesia at 2.5% and O_2 rate at 0.7–0.9 L/min, the lower leg near the posterior ankle was shaved using a fur trimmer and shaving cream. Thereafter, the abovementioned stimulating electrodes were attached using a conductive gel to the posterior ankle at the same place with the simulation modelling. Both stimulation inputs of TENS and ICT were voltage driven.

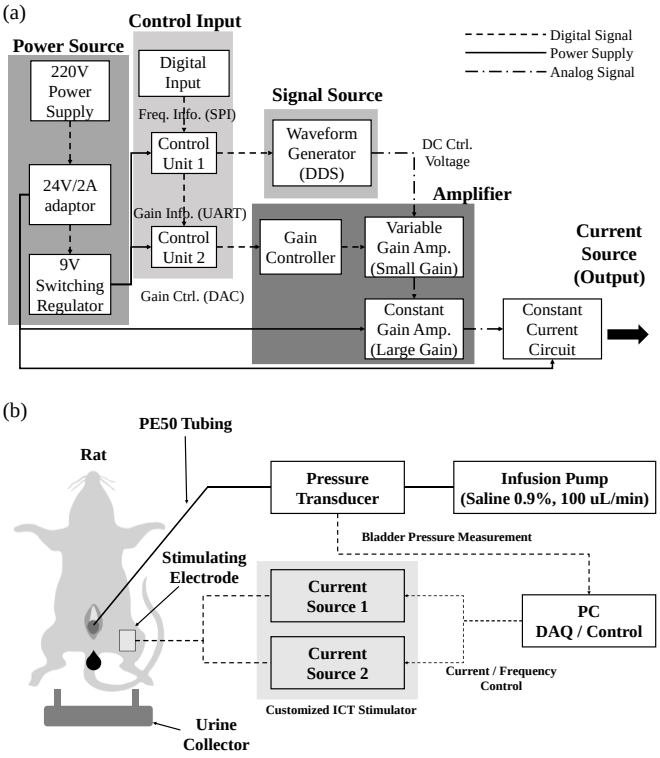

Fig. 4. Systemic illustrations of *in vivo* rat experiments of noninvasive TNS with ICT. (a) Diagram of a customized ICT stimulator. (b) Experimental schematics including the ICT stimulator and bladder activity monitoring system.

F. In Vivo TNS with ICT and TENS

1) Customized ICT Stimulator System

Fig. 4(a) illustrates the operation diagram of a customized ICT stimulator with a current driven circuit. The frequency and current amplitude were controlled using a PC via a customized program (LabVIEW, National Instruments). The output current ranged from 0.1 to 4.4 mA at a voltage bound of ±24 V.

2) Bladder Catheterization

All procedures were approved by the Pohang University of Science and Technology Institutional Animal Care and Use Committee (POSTECH IACUC) for male Sprague–Dawley rats (weight: 250–300 g, just one subject weighed 180 g). For bladder implantation, isoflurane 5%, at a rate of 0.5–0.6 L/min,

was used for short acute anesthesia (2-3 min), after which isoflurane 2% was maintained during surgery (0.5–1 h). Prior to surgery, the rats' abdominal fur was shaved using a hair trimmer and a depilatory cream. The skin was disinfected using isopropyl alcohol (IPA) and povidone. A PE50 tube was catheterized into the bladder, passed under the skin, and retrieved near the neck. Success of the surgery was confirmed by injecting a 0.9% saline solution through the tube and checking whether it emerged of the urethra without leakage. The bladder, muscle, and skin were sutured with braided silk (W593 for bladder and muscle, W529H for skin, Ethicon).

3) Experimental System

Fig. 4(b) visually describes the experimental setup for pre- and post-ICT stimulation bladder activity monitoring. Immediately after surgery, isoflurane was discontinued and urethane (1.0–1.2 g/kg) was injected because isoflurane shows higher MR suppression than urethane [36]. Two half-doses were intraperitoneally injected at 30-min intervals [37]. Upon the occurrence of waking-up signs, a dose of 0.5–1.5 g/kg of urethane was supplemented. For cystometry, the tube pulled out of the subjects' neck was connected to a constant infusing syringe pump (Legato® 210P, KD Scientific) and a pressure transducer (IX-RA-834, iWorx). A 0.9% saline solution was continuously infused (100 μL/min) into the bladder via the catheter, and the subjects were placed on a plate with a urine hole. Urine droplets were naturally collected via the hole onto a Petri dish placed on an electrical scale (HS5002, Hansung Instrument Co.). Bladder pressure and urine weight were continuously transferred to the PC (10 samples/s for the pressure and 0.5 samples/s for the weight). The stimulating electrodes were customized with lead corresponding to the size of the simulation modelling, and they were placed at the same position with the simulation. Two customized ICT current sources were attached with a conductive gel ($\sigma = 0.6\,\mathrm{S/m}$) on the posterior ankle in a location similar to that in the rat simulation model. Current Source 1 used 2 kHz and Current Source 2 used 2.01 kHz, which made a 10 Hz interfering beat frequency.

4) Experimental Protocol

Under anesthesia and solution infusion, the bladder pressure and accumulated urine weight were continuously recorded before stimulation. If passive leakage occurred, indicating abnormal urine discharge caused by the MR suppression due to anesthesia, we waited 0.5–3 h for the disappearance of the suppression. The same constant current was applied to each source, and the current intensity was applied at the level of motor response signs, such as lower leg movement or toe tremor. Stimulation was maintained for 10 min but was withdrawn 30 min after the occurrence of issues such as inappropriate electrode adhesion or when the leg and toe motor signs were too weak. Poststimulation recording was maintained for 0.5–1 h to monitor both the bladder pressure and volume. Before each stimulation, we confirmed that the poststimulation effect totally disappeared and reverted to the prestimulation level to remove the cumulative effect.

5) Analysis

The *average bladder contraction frequency* [aBCF, Contractions/second (C/s)] and *average voiding volume* (aVV, mg) were used to compare pre- and poststimulation bladder activity and to evaluate the stimulating effect of ICT [13, 33, 37]. aBCF was calculated as the number of peaks (5–15 peaks) per time interval between the first and last pre- and poststimulation peaks. aBCF excluded irregulars, such as chaotic peaks, occurring immediately after stimulation (1–10 peaks). Spontaneous contraction peaks indicating nonvoiding contractions were removed by synchronizing the bladder pressure with the cumulative urine weight graph representing the actual voiding activity [38]. The aVV averaged the urine weight per micturition before and after stimulation (5–15 micturition before and after stimulation, except for the chaotic irregulars). The mean ± standard deviation values of both aBCF and aVV before and after stimulation were visualized in bar plots with line graphs connecting each match of "before" and "after" raw data. Wilcoxon's test was used to analyze the statistical difference between the pre- and poststimulation groups. The post-processing analysis and visualization were performed using MATLAB R2017a.

6) Conventional TNS with TENS (Control Group)

To evaluate the physiological effects of ICT–TNS proposed in this study, *in vivo* experiments with conventional TENS–TNS generated by a TENS waveform generator (TPD-NH1, Nu Eyne*)* were performed as a control group. Bladder pressure and voiding volume were recorded using the Powerlab 8/30 system (ADInstruments). The remaining procedure was the same as the above protocols for the experiment using ICT–TNS.

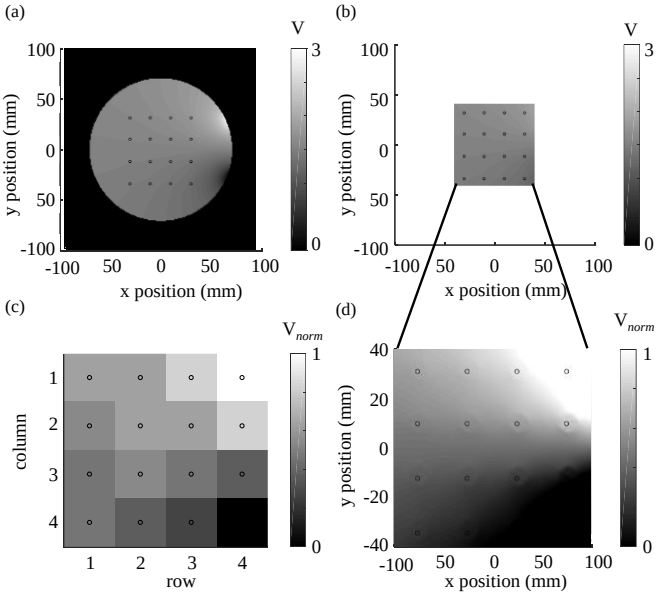

Fig. 5. Simulator validation with *in vitro* phantom experiments. (a) The simulated voltage distribution in 3D phantom model. Each circle indicates the centers of 16 cylinders. (b) and (d) Selectively extracted and normalized simulation data. (c) Normalized measured data from corresponding real phantom.

III. Results

A. Simulator Validation with In Vitro Phantom Experiments

Fig. 5 presents the results of *in vitro* validation. To demonstrate that our simulation framework reflected the

real-world physical environment, the computed distribution of electrical potential was compared with the *in vitro* measurement. Two stimulation electrodes were placed on the right side of the phantom's boundary circle, horizontally symmetric. The lower electrode was set as GND with voltage of 0 V. From the 3D simulation data, a 2D plane where the voltage point electrode is located in the real phantom was selected as in Fig. 5(a). The square region in Fig. 5(b) was extracted from the simulation data to compare with the *in vitro* measured data. The voltage distribution was compared by normalizing both the simulated and measured data with the maximum and minimum value of both experiments. Fig. 5(c) and 5(d) visualize both normalized data. In both, the top-right corner has the highest value, whereas the bottom-right corner has the lowest value. Both the *in silico* and *in vitro* results show the same voltage distribution tendency, which is adequate for validation.

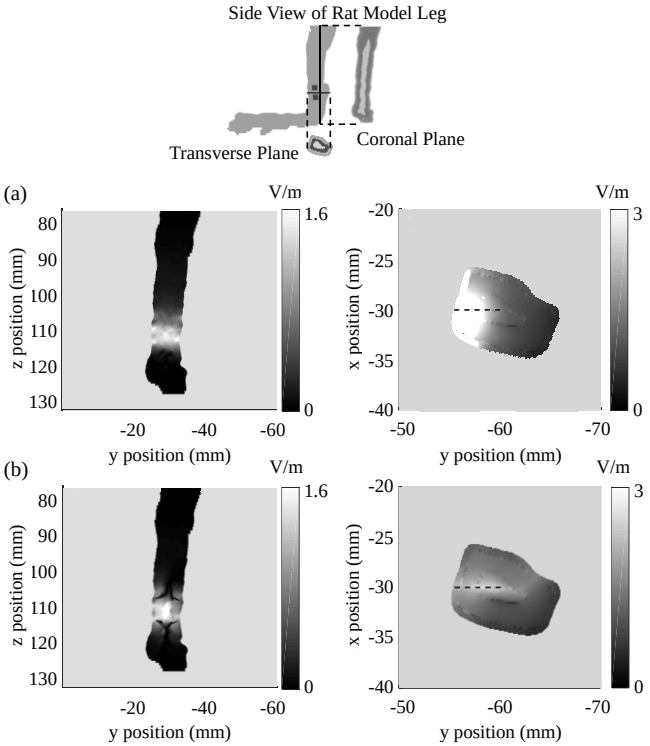

Fig. 6. *In silico* rat experiments comparing ICT with TENS. Top figure illustrates the lower leg of the rat model and slices in transverse and coronal planes. (a) Ez (*z*-axis electric field) distribution of TENS on the coronal plane (left) and on the transverse plane (right). (b) The Ez of ICT on the coronal plane (left) and on the transverse plane (right).

B. In Silico Animal Experiments

Fig. 6 describes the results of the simulation with the 3D rat model comparing TENS and ICT for TNS. The top of Fig. 6 shows a side view of the model's lower leg. The vertical and the horizontal lines designate the locations of a transverse and coronal plane, where the simulated electric field distribution was analyzed. Fig. 6(a) illustrates TENS and Fig. 6(b) illustrates ICT. In both, the right panels represent the Ez linearly scaled from 0 to 1.6 V/m on the coronal plane and the left panels show the Ez from 0 to 3 V/m on the transverse plane.

In the coronal plane, the distribution of Ez of both TENS and ICT have substantial intensities along the *z*-axis in a 10-mm range. Along the y-axis, the difference between the two results was remarkable. The Ez distribution of TENS spreads widely and almost uniformly, whereas the distribution of ICT was specifically focalized inside the deep region.

In the transverse plane, TENS showed that Ez spreads widely, as shown in the coronal plane with high intensity surrounding the stimulation electrodes and skin, which falls sharply after passing the near-skin. On the other hand, ICT shows relatively low field intensity loaded on the near-skin area compared with TENS. Along the y-axis, a long and narrow band was observed that smoothly penetrated from the skin into the inner-body region. The width of the band was <2 mm, demonstrating the focalized tendency of ICT. As a result, ICT passed inside the body without loading an excess of high field on the skin as well as spatially focusing its field.

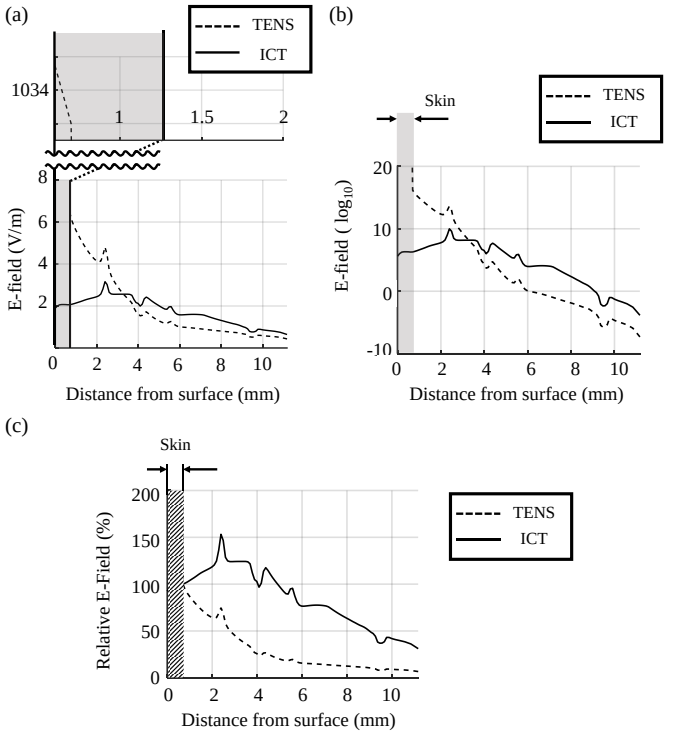

Fig. 7. Line sampled Ez data of TENS and ICT rat simulation results. Dashed line stands for TENS and solid line for ICT. Skin area is painted with gray color. (a) Linear scale E-field; (b) Logarithmic scale E-field; and (c), Relative E-field based on the field just beneath the skin

Fig. 7 shows data sampled from the focused band of the ICT and TENS-induced fields on the transverse plane. The location of the sample data is marked with the black dashed line in Fig. 6. The TENS has an extremely high near-skin field and extremely low inner-body field, whereas the ICT shows not much lower near-skin field intensity but higher inner-body field than TENS (see Fig. 7(a)). The inner-body field difference between TENS and ICT is more remarkable in logarithmic scale, as shown in Fig. 6(b). The ICT field intensity is approximately 1.56 times higher than that of TENS near the tibial nerve (5-mm deep under the skin). Fig. 6(c) presents that the relative electric field, based on the near-skin field, is considerably larger for ICT than for TENS. The ICT field maintained >90% intensity near the tibial nerve compared with that near the skin, whereas the

TENS field reduced to 20%. Moreover, ICT has its maximum field inside the body and not near the skin due to the focusing property.

C. In Vivo Animal Experiments

1) Comparison of Stimulation Threshold between ICT and TENS

Fig. 8(a) illustrates the differences in the stimulation threshold between TENS–TNS and ICT–TNS for tibial nerve excitation (n = 18 for each group). The results were plotted in bar plots with standard deviation. For TENS, the stimulation threshold was 10.7 ± 3.80 V (mean ± standard deviation). For ICT, the threshold was 6.4 ± 1.5 V. Therefore, the mean of stimulation threshold for ICT–TNS was approximately 1.67 times lower than that for TENS–TNS (p < 0.001). Fig. 8(b) plots the XY distribution of the stimulation thresholds of TENS and ICT. The least square regression line of the data has much smaller slope (0.38) than the Y=X baseline (slope: 1). Furthermore, the coefficient of determination (R^2) between the stimulation thresholds of TENS and ICT was 0.8973.

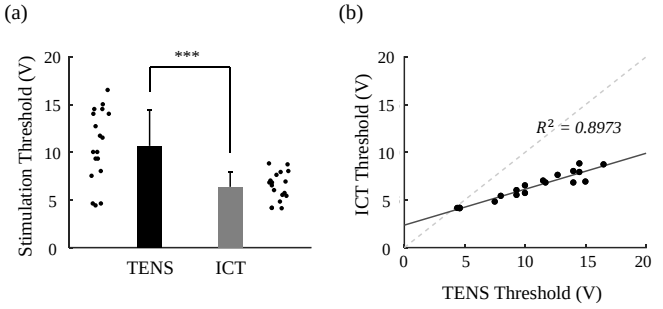

Fig. 8. Comparison of stimulation thresholds of TENS and ICT. (a) Bar plots of voltage stimulation thresholds of TENS and ICT. Black dots present raw data. (b) XY plot of the thresholds of TENS and ICT. Dashed gray line indicates that the TENS and ICT thresholds are the same. Black solid line is the least square regression line of the data. (Unpaired t−test for (a), $^{***}\boldsymbol{p}$ < 0.001. $\boldsymbol{n}$ = 18 for each TENS and ICT group)

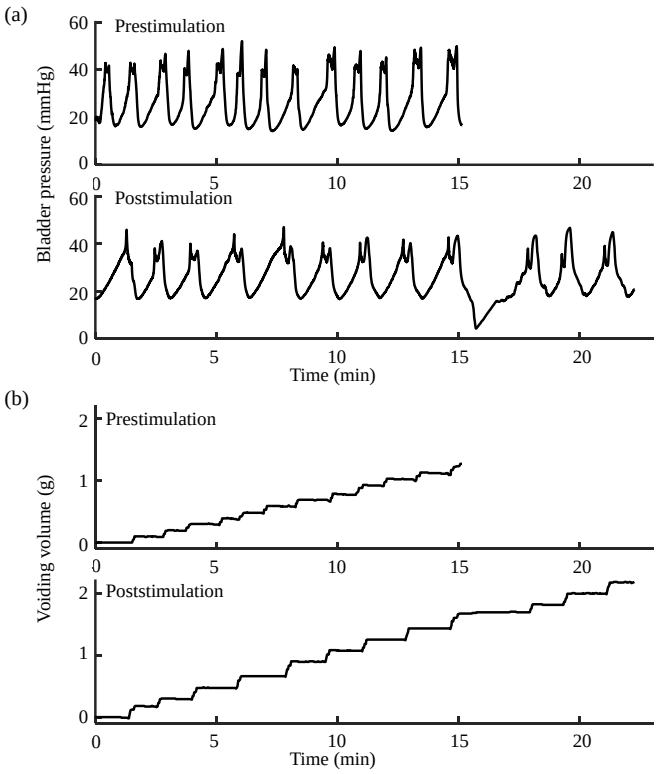

Fig. 9. Continuous bladder pressure and cumulative voiding volume before and after ICT stimulation on the posterior ankle of rats. (a) Bladder pressure monitoring for 13 periods of micturition reflexes (urination). (b) Voiding volume for the corresponding reflexes.

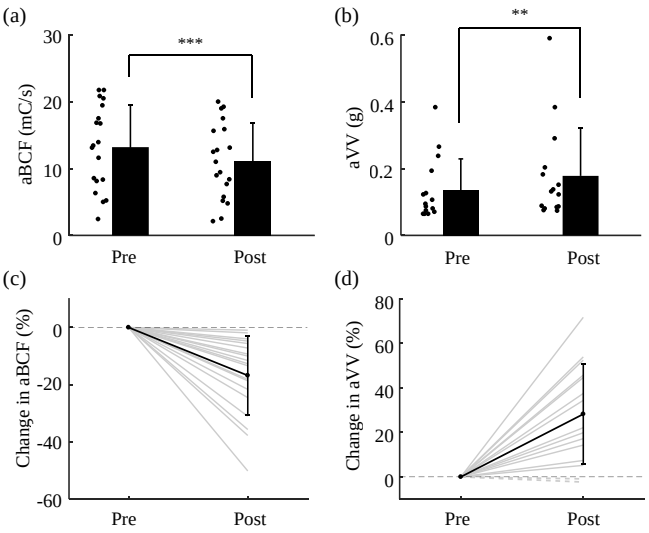

Fig. 10. Mean bladder contraction frequency (aBCF) and mean voiding volume (aVV) for pre- and poststimulation of ICT. (a)−(b) Bar plots (mean ± standard deviation) of aBCF and aVV before and after ICT stimulation; (a) aBCF, (b) aVV. Black dots present raw data. (c)−(d) Percentile changes of aBCF and aVV after stimulation; (c) aBCF, (d) aVV. Full data set is superimposed in gray. Mean and standard deviation of the changes are covered in black. (Wilcoxon signed-ranked test for (a) and (b): $^{**}\boldsymbol{p}$ < 0.01, $^{***}\boldsymbol{p}$ < 0.001, $\boldsymbol{n}$ = 19 for aBCF and $\boldsymbol{n}$ = 15 for aVV)

2) Rat Cystometry with the ICT for TNS

Experimental data of bladder pressure and voiding volume were obtained from 8 out of 9 rats. Data from 1 rat were excluded because of unknown bladder pressure pattern with continuously increasing baseline. Fig. 9 shows the representative bladder pressures and voiding volumes measured during pre- and poststimulation. Fig. 9(a) shows sampled data of pressure for 13 MR peaks, and Fig. 9(b) shows the corresponding cumulative voiding volume. In both figures, the upper graph represents the prestimulation data, whereas the lower graph represents the poststimulation data. An MR period was defined as an interval between two continuous peaks. Starting from the first peak, there were 12 peak-to-peak

TABLE II
AVERAGE BLADDER CONTRACTION FREQUENCY AND AVERAGE VOIDING VOLUME IN PRE AND POST STIMULATION

n = 19	aBCF	
	Mean ± std.	mean of change
Pre	13.2 ± 6.3 mC/s	−16.8 %
Post	11.1 ± 5.7 mC/s	

n = 15	aVV	
	Mean ± std.	mean of change
Pre	135 ± 94 mg	7.38 %
Post	178 ± 14 mg	

intervals. The prestimulation pressure lasted for approximately 15 min of the total 12 periods, and the corresponding volume was approximately1.3 g. After stimulation, the total time was about 20 min and the total volume was approximately 2.2 g. The aBCF decreased from 14 to 9 mC/s, and the aVV increased from 110 to 180 mg. The change in aBCF and aVV was −36% and 72%, respectively.

For all experiments, Table II shows the mean aBCF (n = 19) and aVV (n = 15) with standard deviation and mean of change between pre- and poststimulation in aBCF and aVV. The lack of four aVV samples compared to aBCF was due to instrumental issues from the first 3 rats. The mean of aBCF decreased by approximately 17%, and that of aVV increased by approximately 7%. Fig. 10 complements the table with raw data and statistical analysis. Fig. 10(a) and 10(c) represent that the aBCF decrease is meaningful ($p < 0.001$), ranging from −0.94% at least to −50% at most. Fig. 10(b) and 10(d) represent that an aVV increase is also verified ($p < 0.01$), ranging from −2.3% to 72%.

Fig. 11 shows other observed bladder activity changes caused by TNS with ICT. Fig. 11(a) and 11(c) show that MRs were lost during or after stimulation. These are characterized as increasing the bladder pressure baseline and deleting the contraction peaks strictly related to passive leakages. In Fig. 11(b), the contraction peak amplitudes were reduced during the stimulation phase. These irregular changes were observed from only one sample thorughout the entire experiment.

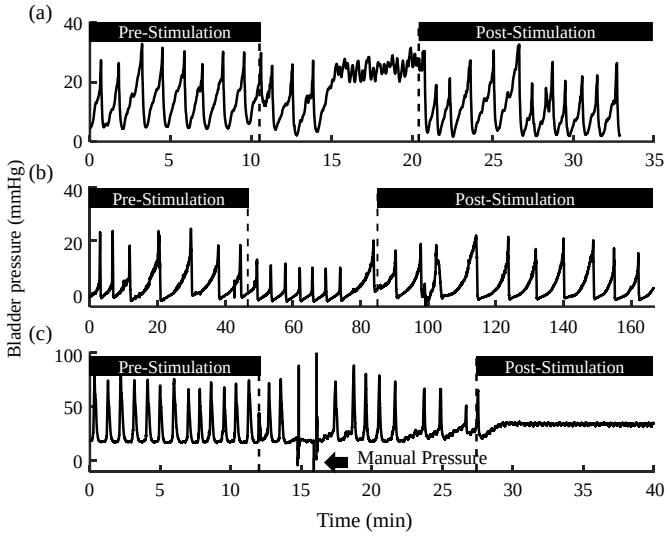

Fig. 11. Other observed changes in bladder pressure after ICT stimulation. Unclassified observations of change in bladder pressure after ICT stimulation. (a) Passive leakage occurred during the stimulation. (b) Reduced contraction pressure amplitude during the stimulation. (c) Passive leakage occurred during stimulation and last after the stimulation. (only $\boldsymbol{n}$ = 1 for each of (a), (b), and (c))

3) Comparison of Rat Cystometry between ICT and TENS

Fig. 12 presents a comparison between the physiological effects of ICT (experimental group) and TENS (controlled group), illustrating the difference in changes in physiological bladder activity between TENS–TNS and ICT–TNS in terms of aBCF and aVV (n = 10 for aBCF and aVV of TENS, n = 19 for aBCF of ICT and n = 15 for aVV of ICT). Fig. 12(a) shows a slight difference in the median of change in aBCF between ICT (−12.7 %) and TENS (−11.0 %) (p = 0.226). For the change in aVV shown in Fig. 11(b), the overall distribution of ICT was located higher than that of TENS as well as the median of aVV changes of ICT (+22 %) was higher than that of TENS (+7.1 %) (p = 0.068).

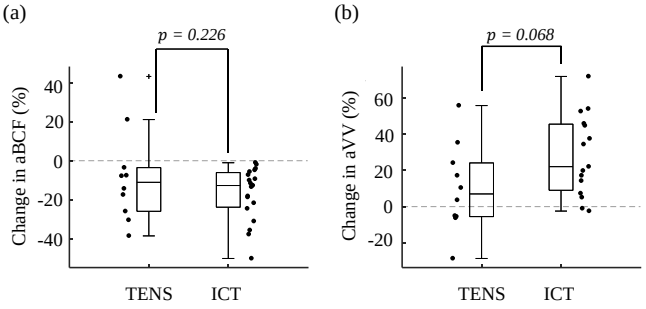

Fig. 12. Comparison of bladder activity changes after TENS and ICT. (a)–(b) Boxplots of poststimulation-induced bladder activity change of TENS and ICT; (a) Percentile changes in aBCF, (b) Percentile changes in aVV. Black dots present raw data. (Unpaired t−test, $\boldsymbol{n}$ = 10 for TENS in both of (a) and (b), $\boldsymbol{n}$ = 19 for ICT in (a) and $\boldsymbol{n}$ = 15 for ICT in (b))

D. In Silico Human Experiments

Fig. 13 shows an overview of the *in silico* human model simulation results. Fig. 13(a) illustrates the positions of stimulating electrodes for TENS and ICT, and the location of the tibial nerve on cross-sectional views of coronal and transverse planes. The planar graphs in Fig. 13(b) and (c) are on the coronal and transverse planes and illustrate the calculated distributions of Ez of the TENS. The graphs of Fig. 13(d) and (f) are on the same plane but illustrate the distribution of Ez of the ICT. In the coronal plane (Fig. 13(b) and (d)), the overall distribution of Ez of ICT shows a stronger and focused intensity than that of TENS. The transverse plane of TENS in Fig. 13(c) shows a widely spread and extremely strong Ez around the skin, and it is sharply dissipated as penetrating inside the body. However, ICT generates a comparatively focused band and transfers the electric field to deeper regions without considerable dissipation (Fig. 13(e)). Therefore, the inner-body electric field generated by ICT around the tibial nerve is stronger than that generated by TENS.

Sampled data from the simulation results clearly differentiate the inner field intensity of TENS and ICT (Fig. 13(f)). For sampling, line data were extracted along the gray dashed lines in Fig. 13(c) and (e), penetrating from the near-skin surface to inner-body deep region. The location of the tibial nerve is marked with black circle on the lines. TENS has near-skin intensity of 7.0 V/m, whereas the intensity of ICT is approximately 1.1 V/m, which is considerably lower than that of TENS. However, the near-tibial field (inner-body field) intensity of ICT is higher than that of TENS. In particular, the ICT has the highest value inside the body and not in the superficial region. In contrast, the TENS field is much stronger than the ICT in the superficial region. However, the TENS intensity reduced to 0.62 V/m and the ICT intensity slightly

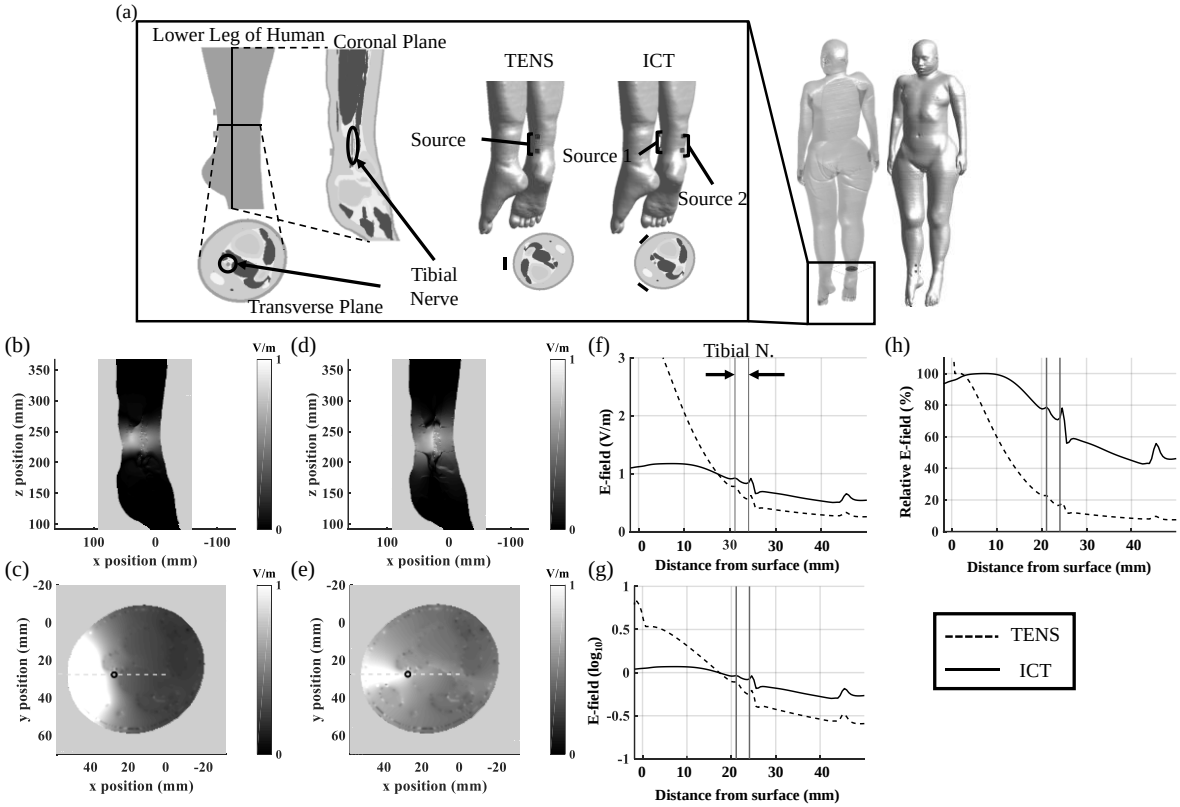

Fig. 13. *In silico* human experiments comparing ICT and TENS. (a) 3D human model with stimulating electrodes for TENS and ICT on the posterior ankle. Location of the tibial nerve is marked in cross-sections of a coronal and a transverse plane. (b) Distribution of Ez generated by TENS on the coronal plane, and (c) on the transverse plane. The black circle points the position of tibial nerve. (d) Ez distribution by ICT compared to TENS on the coronal plane, and (d) on the transverse plane. (f) & (g) Linear and logarithmic scale graphs of line sampled Ez data along the dashed line of (c) and (e). (h) Relative Ez based on each maximum value of TENS and ICT. The location of the tibial nerve is marked with horizontal lines and arrows in (f)−(h)

decreased only to 0.85 V/m at the tibial nerve. The intensity difference between TENS and ICT was more clearly illustrated in logarithmic scale as shown in Fig. 13(g). Fig. 13(h) presents the relative value of the inner-body field at the tibial nerve over the near-skin field. Compared with the near-skin field, the inner-body field intensity of TENS decreased to 20% but the ICT intensity decreased only to 80%. ICT intensity was its maximum not near the skin but inside the body

IV. Discussion and Conclusion

The proposed ICT modality is similar to the conventional TENS in that both methods are based on noninvasive transcutaneous delivery of electric fields for nerve stimulation. However, their field penetration efficiencies are quite different because the ratio of inner-body field to near-skin field generated by ICT is considerably higher than that generated by TENS. This is because the electrical impedance of the subcutaneous tissue is much lower at the carrier frequency of ICT than at that of TENS (which is technically direct current). Although high-frequency signals are filtered by neuron membranes, ICT can successfully cause stimulation and elicit physiological response using the low-frequency beat envelope. We evaluated and verified the field penetration efficiency and physiological effectiveness of ICT and compared their performances with conventional TENS applied for OAB treatment.

In vivo measurements of inner-body field relative to near-skin field comprise the best and most direct way to evaluate the field penetration efficiency. However, this requires the insertion of recording electrodes into tissues, causing severe damage and electrical parameter distortion. In addition, conventional analytical calculation is almost impossible due to the complex heterogeneity of body tissues. Therefore, we used a 3D *in silico* model to characterize and analyze the difference of field penetration efficiency between the ICT- and TENS-induced electric fields. Before using the simulation framework for prediction, we extensively validated the computational model *in vitro* by showing the excellent agreement between the measured and simulation results (Fig. 5).

The *in silico* experiments showed a distinctly high penetration efficiency of ICT because the relative value of the field near the tibial nerve to the field near the skin was extremely high (Fig 7 and 13). In contrast, TENS showed extremely low penetration efficiency with much smaller relative value than that showed by ICT. The difference in their penetration efficiencies permitted for ICT to load less energy near the skin for the same level of tibial nerve recruitment with TENS. In other words, compared with TENS, ICT could transfer a stronger field to the tibial nerve deep inside the body with less power attenuation near the subcutaneous area. This implies that ICT–TNS shows more efficient penetration into the body deep near the tibial nerve as well as mitigates the skin-related safety issue of TENS–TNS.

Subsequent *in vivo* experiments measuring the stimulation thresholds of ICT–TNS and TENS–TNS showed that the ICT modality has much lower threshold to evoke and stimulate the tibial nerve than that of TENS (Fig. 8). The mean stimulation threshold of ICT–TNS was 1.67 times lower than that of TENS–TNS, which is plausibly related to the mean simulation result that the electric field of ICT was 1.56 times higher than that of TENS. The results demonstrated that ICT can transfer the stimulation field to the inner-body nerve 1.5–1.7 times easily than TENS. This indicates that the ICT modality is safer and more efficient than the conventional TENS modality due to its high penetration efficiency.

The physiological effectiveness of ICT–TNS for bladder function control was demonstrated using preclinical animal studies. Cystometry, the conventional bladder-function evaluation method with bladder pressure and voiding volume of urine, continuously monitored and featured the bladder contraction (urination) moments after the ICT–TNS [36-38]. The results shown in Fig. 9 and 10 statistically verify the bladder activity changes after the ICT–TNS, as bladder contraction frequency decreased and voiding volume increased. These results indicate that the low-frequency envelope of ICT successfully inhibited the bladder activity and controlled the function by increasing bladder capacity and decreasing urination frequency.

In addition, by comparing the clinical performance of ICT–TNS with that of conventional TENS–TNS, ICT–TNS showed similar or same effectiveness in treating bladder contraction and voiding volume compared with TENS–TNS (Fig. 12). This performance on bladder control by ICT–TNS shows the physiological effectiveness of ICT–TNS for OAB therapy by relieving its representative symptoms of bladder capacity decrease and the subsequent urinary urgency. Therefore, the clinical potential of ICT–TNS for OAB treatment can be proposed owing to its superiority on high penetration efficiency as well as the good physiological effectiveness from the preclinical study results.

Despite its clinical potential, it is important to acknowledge that future studies may be required for improving the proposed modality by optimizing the ICT stimulation parameters. Adjusting ICT-related parameters, such as electrode positioning and carrier frequency, is expected to optimize the penetration depth and focusing region of ICT for TNS in OAB therapy. Particularly, the optimization for electrode placement is expected to increase the focusing and targeting ability of ICT–TNS for maximizing the tibial nerve recruitment. The *in silico* experiment results (Fig. 7 and 13) confirm the potential for the optimization because the focused ICT electric field is not maximized at the tibial nerve. Further, the optimization should consider the electrode placement that is least influenced by anatomical heterogeneity for the real world clinical application because such heterogeneity results in the variances of the target location and focusing resolution. Moreover, the optimization of ICT–TNS could prevent the side effects of TNS itself, such as passive leakage presented in Fig. 11, which is expected due to sphincter dysfunction. Therefore, future studies are required to evaluate the different effectiveness of ICT according to the various electrode placements.

Preclinical studies encompassing larger and more human-like animals, such as porcine and canine subjects, may strengthen the clinical effectiveness of the ICT. Even based on its clinical safety and experimental ease, clinical studies with human volunteers could be considered for future research because ICT–TNS is noninvasive and has no severe side effects, thereby being sufficiently safe for human studies.

In conclusion, this study proposes a new modality for noninvasive TNS using time interfering current method called ICT, increasing the field penetration efficiency of TNS, thereby preventing the side effects of conventional TENS–TNS. Computational analysis with electromagnetic biomedical modeling demonstrated the increased field penetration efficiency of TNS by applying ICT. *In vivo* animal experiments proved the superior penetration efficiency of ICT–TNS via the lower stimulation threshold of ICT than TENS as well as proved the good physiological effectiveness of ICT–TNS in terms of the bladder inhibition compared with the clinical performance of TENS–TNS. Therefore, ICT method is expected to be applied in several other noninvasive peripheral nerve stimulation therapies as well as TNS to treat OAB.

REFERENCES

[1] M. J. Kennelly, and W. B. DeVoe, "Overactive bladder: pharmacologic treatments in the neurogenic population," *Reviews in Urology,* vol. 10, no. 3, pp. 182, 2008.

[2] S. A. MacDiarmid, "The evolution of transdermal/topical overactive bladder therapy and its benefits over oral therapy," *Reviews in Obstetrics and Gynecology,* vol. 2, no. 2, pp. 116, 2009.

[3] W. S. Reynolds *et al.*, "The burden of overactive bladder on US public health," *Current Bladder Dysfunction Reports,* vol. 11, no. 1, pp. 8-13, 2016.

[4] R. R. Dmochowski, and D. K. Newman, "Impact of overactive bladder on women in the United States:results of a national survey," *Current Medical Research and Opinion,* vol. 23, no. 1, pp. 65-76, 2007/01/01, 2007.

[5] K. S. Coyne *et al.*, "Comorbidities and personal burden of urgency urinary incontinence: a systematic review," *International Journal of Clinical Practice,* vol. 67, no. 10, pp. 1015-1033, 2013.

[6] W. C. de Groat, "A neurologic basis for the overactive bladder," *Urology,* vol. 50, no. 6, pp. 36-52, 1997.

[7] J. Arnold *et al.*, "Overactive bladder syndrome: management and treatment options," *Australian Family Physician,* vol. 41, no. 11, pp. 878, 2012.

[8] S. Srikrishna *et al.*, "Management of overactive bladder syndrome," *Postgraduate Medical Journal,* vol. 83, no. 981, pp. 481, 2007.

[9] K. E. Andersson, "Current concepts in the treatment of disorders of micturition," *Drugs,* vol. 35, no. 4, pp. 477-494, April 01, 1988.

[10] R. A. Schmidt *et al.*, "Sacral nerve stimulation for treatment of refractory urinary urge incontinence," *The Journal of Urology,* vol. 162, no. 2, pp. 352-357, 1999.

[11] M. Slovak *et al.*, "Non-invasive transcutaneous electrical stimulation in the treatment of overactive bladder," *Asian Journal of Urology,* vol. 2, no. 2, pp. 92-101, 2015/04/01/, 2015.

[12] Z. Guo *et al.*, "Transcutaneous electrical nerve stimulation in the treatment of patients with poststroke urinary incontinence," *Clinical Interventions in Aging,* vol. 9, pp. 851, 2014.

[13] U. Jonas *et al.*, "Efficacy of sacral nerve stimulation for urinary retention: results 18 months after implantation," *The Journal of Urology,* vol. 165, no. 1, pp. 15-19, 2001.

[14] S. W. Siegel *et al.*, "Long-term results of a multicenter study on sacral nerve stimulation for treatment of urinary urge incontinence, urgency-frequency, and retention," *Urology,* vol. 56, no. 6, Supplement 1, pp. 87-91, 2000/12/01/, 2000.

[15] M. Brazzelli *et al.*, "Efficacy and safety of sacral nerve stimulation for urinary urge incontinence: a systematic review," *The Journal of Urology,* vol. 175, no. 3, pp. 835-841, 2006/03/01/, 2006.

[16] L. L. de Wall, and J. P. Heesakkers, "Effectiveness of percutaneous tibial nerve stimulation in the treatment of overactive bladder syndrome," *Research and reports in urology,* vol. 9, pp. 145-157, 2017.
[17] A. Lee *et al.*, "Stimulation of the wrist acupuncture point PC6 for preventing postoperative nausea and vomiting," *The Cochrane Database of Systematic Reviews,* vol. 11, no. 11, 2015.
[18] T. Yamanishi *et al.*, "Neuromodulation for the treatment of lower urinary tract symptoms," *LUTS: Lower Urinary Tract Symptoms,* vol. 7, no. 3, pp. 121-132, 2015.
[19] T. Yamanishi *et al.*, "Neuromodulation for the treatment of urinary incontinence," *International Journal of Urology,* vol. 15, no. 8, pp. 665-672, 2008.
[20] N. Grossman *et al.*, "Noninvasive deep brain stimulation via temporally interfering electric fields," *Cell,* vol. 169, no. 6, pp. 1029-1041. e1016, 2017.
[21] L. E. Medina, and W. M. Grill, "Nerve excitation using an amplitude-modulated signal with kilohertz-frequency carrier and non-zero offset," *Journal of Neuroengineering and Rehabilitation,* vol. 13, no. 1, pp. 63, 2016.
[22] B. Hutcheon, and Y. Yarom, "Resonance, oscillation and the intrinsic frequency preferences of neurons," *Trends in Neurosciences,* vol. 23, no. 5, pp. 216-222, 2000/05/01/, 2000.
[23] L. Schreiner *et al.*, "Randomized trial of transcutaneous tibial nerve stimulation to treat urge urinary incontinence in older women," *International Urogynecology Journal,* vol. 21, no. 9, pp. 1065-1070, September 01, 2010.
[24] C. W. Elder, and P. B. Yoo, "A finite element modeling study of peripheral nerve recruitment by percutaneous tibial nerve stimulation in the human lower leg," *Medical Engineering & Physics,* vol. 53, pp. 32-38, 2018/03/01/, 2018.
[25] C. A. Balanis, "Advanced engineering electromagnetics" 2nd ed., ch. 2, pp. 39-98, Hoboken, N.J.: John Wiley & Sons, 2012.
[26] X. L. Chen *et al.*, "Low frequency electromagnetic field exposure study with posable human body model," *2010 IEEE International Symposium on Electromagnetic Compatibility,* pp. 702-705, July 25-30, 2010.
[27] M. Vöröslakos *et al.*, "Direct effects of transcranial electric stimulation on brain circuits in rats and humans," *Nature Communications,* vol. 9, no. 1, pp. 483, 2018/02/02, 2018.
[28] C. Gabriel, "Compilation of the dielectric properties of body tissues at RF and microwave frequencies," AL/OE-TR-1996-0037, Brooks Air Fore Base, Texas, 1996.
[29] C. Gabriel *et al.*, "Electrical conductivity of tissue at frequencies below 1 MHz," *Physics in Medicine and Biology,* vol. 54, no. 16, pp. 4863-4878, 2009/07/27, 2009.
[30] J. S. Park *et al.*, "Visible Korean human: improved serially sectioned images of the entire body," *IEEE Transactions on Medical Imaging,* vol. 24, no. 3, pp. 352-360, 2005.
[31] H. S. Park *et al.*, "Improved sectioned images and surface models of the whole dog body," *Annals of Anatomy - Anatomischer Anzeiger,* vol. 196, no. 5, pp. 352-359, 2014/09/01/, 2014.
[32] W. Kainz *et al.*, "Development of novel whole-body exposure setups for rats providing high efficiency, National Toxicology Program (NTP) compatibility and well-characterized exposure," *Physics in Medicine and Biology,* vol. 51, no. 20, pp. 5211-5229, 2006/09/27, 2006.
[33] G. Amarenco *et al.*, "Urodynamic effect of acute transcutaneous posterior tibial nerve stimulation in overactive bladder," *The Journal of Urology,* vol. 169, no. 6, pp. 2210-2215, 2003/06/01/, 2003.
[34] M. de Sèze *et al.*, "Transcutaneous posterior tibial nerve stimulation for treatment of the overactive bladder syndrome in multiple sclerosis: Results of a multicenter prospective study," *Neurourology and Urodynamics,* vol. 30, no. 3, pp. 306-311, 2011.
[35] B. J. Roth, and P. J. Basser, "A model of the stimulation of a nerve fiber by electromagnetic induction," *IEEE Transactions on Biomedical Engineering,* vol. 37, no. 6, pp. 588-597, 1990.
[36] H. Y. Chang, and L. A. Havton, "Differential effects of urethane and isoflurane on external urethral sphincter electromyography and cystometry in rats," *American Journal of Physiology-Renal Physiology,* vol. 295, no. 4, pp. F1248-F1253, 2008.
[37] M. Kovacevic, and P. B. Yoo, "Reflex neuromodulation of bladder function elicited by posterior tibial nerve stimulation in anesthetized rats," *American Journal of Physiology-Renal Physiology,* vol. 308, no. 4, pp. F320-F329, 2015.
[38] T. W. C. M.D, and M. S. D. Ph.D, "Effects of anesthesia on cystometry and leak point pressure of the female rat," *Life Sciences,* vol. 69, no. 10, pp. 1193-1202, 2001/07/27/, 2001.